# Reports

## Optical Coherence Tomography

DAVID HUANG, ERIC A. SWANSON, CHARLES P. LIN, JOEL S. SCHUMAN, WILLIAM G. STINSON, WARREN CHANG, MICHAEL R. HEE, THOMAS FLOTTE, KENTON GREGORY, CARMEN A. PULIAFITO, JAMES G. FUJIMOTO*

**A technique called optical coherence tomography (OCT) has been developed for noninvasive cross-sectional imaging in biological systems. OCT uses low-coherence interferometry to produce a two-dimensional image of optical scattering from internal tissue microstructures in a way that is analogous to ultrasonic pulse-echo imaging. OCT has longitudinal and lateral spatial resolutions of a few micrometers and can detect reflected signals as small as $\sim 10^{-10}$ of the incident optical power. Tomographic imaging is demonstrated in vitro in the peripapillary area of the retina and in the coronary artery, two clinically relevant examples that are representative of transparent and turbid media, respectively.**

TOMOGRAPHIC IMAGING TECHniques such as x-ray computed tomography (*1*), magnetic resonance imaging (*2*), and ultrasound imaging (*3*) have found widespread applications in medicine. Each of these techniques measures a different physical property and has a resolution and penetration range that prove advantageous for specific applications. In this report, we discuss OCT. With this technique it is possible to perform noninvasive cross-sectional imaging of internal structures in biological tissues by measuring their optical reflections.

Both low-coherence light and ultrashort laser pulses can be used to measure internal structure in biological systems. An optical signal that is transmitted through or reflected from a biological tissue will contain time-of-flight information, which in turn yields spatial information about tissue microstructure. Time-resolved transmission spectroscopy has been used to measure absorption and scattering properties in tissues and has been demonstrated as a noninvasive diagnostic measure of hemoglobin oxygenation in the brain (*4*). Optical ranging measurements of microstructure have been performed in the eye and the skin with femtosecond laser pulses (*5*). Time gating by means of coherent (*6*) as well as noncoherent (*7*) techniques has been used to preferentially detect directly transmitted light and obtain transmission images in turbid tissue. Low-coherence reflectometry has been used for ranging measurements in optical components (*8*), for surface contour mapping in integrated circuits (*9*), and for ranging measurements in the retina (*10*) and other eye structures (*10, 11*).

In contrast to time domain techniques, low-coherence reflectometry can be performed with continuous-wave light without the need for ultrashort pulse laser sources. Furthermore, recent technological advances in low-coherence reflectometry have allowed the construction of compact and modular systems that use diode light sources and fiber optics and have achieved micrometer spatial resolutions and high detection sensitivities (*12*).

We have extended the technique of low-coherence reflectometry to tomographic imaging in biological systems. In low-coherence reflectometry, the coherence property of light reflected from a sample provides information on the time-of-flight delay from the reflective boundaries and backscattering sites in the sample. The delay information is then used to determine the longitudinal location of the reflection sites. The OCT system performs multiple longitudinal scans at a series of lateral locations to provide a two-dimensional map of reflection sites in the sample. This mode of operation is analogous to ultrasonic pulse-echo imaging (ultrasound B-mode).

The optical sectioning capability of OCT is akin to that of confocal microscopic systems (*13, 14*). However, although the longitudinal resolution of confocal microscopy depends on the available numerical aperture (*15*), OCT's resolution is limited only by the coherence length of the light source. Thus, OCT can maintain high depth resolution even when the available aperture is small. This feature will be particularly useful for in vivo measurement of deep tissues, for example, in transpupillary imaging of the posterior eye and in endoscopic imaging.

The OCT scanner (Fig. 1) is an extension of previous low-coherence reflectometer systems (*12*). High-speed, continuous-motion longitudinal scanning is used to increase the data acquisition rate, and a transverse scanning mechanism makes possible two-dimensional imaging. The heart of the system is the fiber optic Michelson interferometer, which is illuminated by low-coherence light (830 nm wavelength) from a superluminescent diode (SLD). The tissue sample is placed in one interferometer arm, and sample reflections are combined with the reflection from the reference mirror. The amplitudes and delays of tissue reflections are measured by scanning the reference mirror

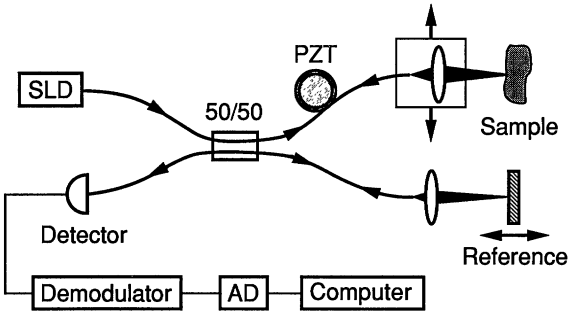


**Fig. 1.** Schematic of the OCT scanner. The SLD output is coupled into a single mode fiber and split at the 50/50 coupler into sample and reference arms. Reflections from the two arms are combined at the coupler and detected by the photodiode. Longitudinal scanning is performed by translating the reference mirror with a stepper motor stage at 1.6 mm $s^{-1}$, generating a 3.8-kHz Doppler shift. The piezoelectric transducer (PZT) in the sample arm further provides 21.2-kHz phase modulation to the interferometric signal. Interferometric modulation of the output intensity is detected by the photodetector when the reference and sample arm delays are nearly matched. The detector output is demodulated at the sum modulation frequency of 25 kHz to produce the envelope of the interferometric signal, which is then digitized (AD) and stored on computer. A series of longitudinal scans are performed. The lateral beam position is translated after each longitudinal scan.

D. Huang, M. R. Hee, J. G. Fujimoto, Department of Electrical Engineering and Computer Science and Research Laboratory of Electronics, Massachusetts Institute of Technology, Cambridge, MA 02139.
E. A. Swanson, Lincoln Laboratory, Massachusetts Institute of Technology, Lexington, MA 02139.
C. P. Lin, J. S. Schuman, W. G. Stinson, W. Chang, C. A. Puliafito, Department of Ophthalmology, Harvard Medical School and the Laser Research Laboratory, Massachusetts Eye and Ear Infirmary, Boston, MA 02114.
T. Flotte and K. Gregory, Wellman Laboratories, Massachusetts General Hospital, Boston, MA 02114.

*To whom correspondence should be addressed.

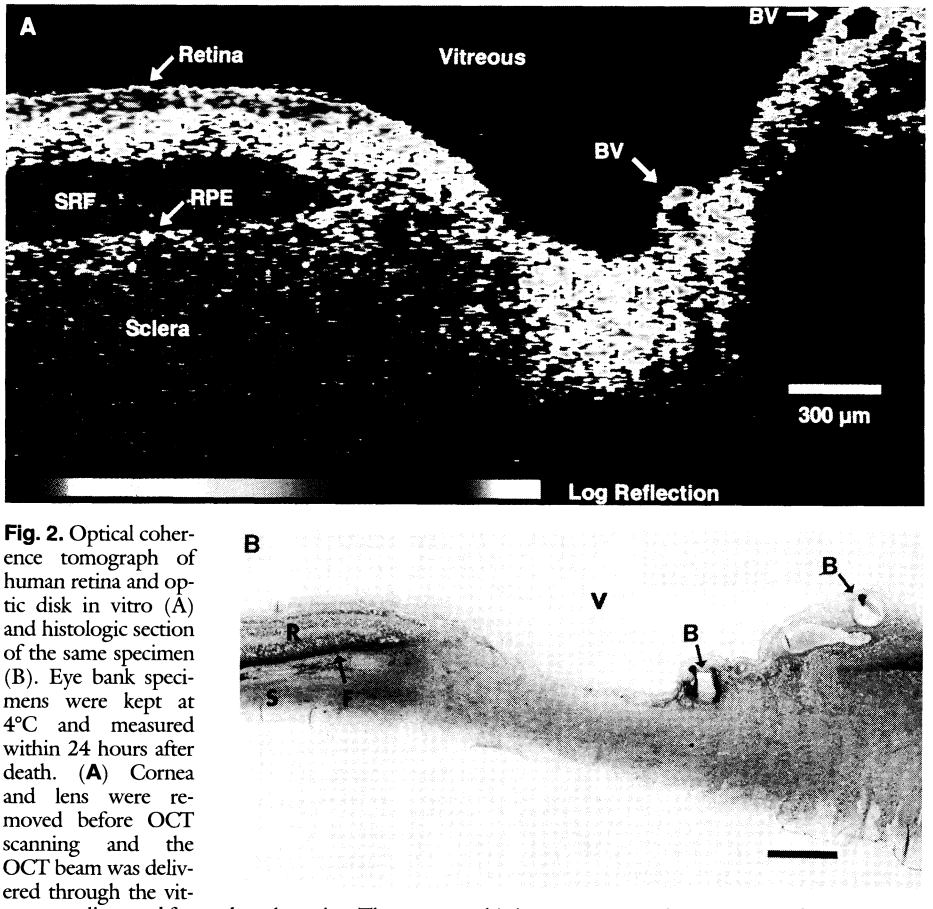


**Fig. 2.** Optical coherence tomograph of human retina and optic disk in vitro (A) and histologic section of the same specimen (B). Eye bank specimens were kept at 4°C and measured within 24 hours after death. (**A**) Cornea and lens were removed before OCT scanning and the OCT beam was delivered through the vitreous medium and focused on the retina. The tomographic image corresponds to a section of the retina and optic disk along the papillomacular axis. The retina temporal to the disk is on the left. Identifiable structures are, from top to bottom, vitreous, retina (RNFL, red; subjacent retina, yellow to light blue), subretinal fluid (SRF), retinal pigment epithelium (RPE), and choroid and sclera. The RNFL thickness varies between 70 and 90 μm, increasing toward the optic disk. The overall retinal thickness is 220 μm. Blood vessels (BV) in the optic disk appear as characteristic dark spots. The nasal retina appears on the far right. The sampled pixel size is 3.8 (vertical) by 20 (horizontal) μm. Interpolation between pixels was performed to improve image readability. The color scale spans $4 \times 10^{-10}$ (black) to $10^{-6}$ (white) of the incident power. (**B**) Stevenol's blue–stained plastic section. The RNFL and overall retinal thickness closely match those of the tomograph; the SRF is much smaller than in the tomograph because of dehydration during histologic processing. Vitreous (V), retina (R), sclera (S), blood vessel (B), SRF (F). Bar = 300 μm.

position and simultaneously recording the amplitude of the interferometric signal. Interferometric signal is detected only when the reflections from the sample and reference arms of the interferometer are nearly matched in group delay (time-of-flight). Because of the low coherence, the signal falls off rapidly with delay mismatch and the delay or longitudinal location of sample reflections can be determined with high resolution.

In our system, the full-width–half-maximum (FWHM) longitudinal resolution was 17 μm in air. The position of reflective boundaries inside a sample can usually be measured with much higher accuracy than the FWHM figure. In the absence of strong nearby reflections, the origin of a sample reflection can be repeatably located with a spatial resolution of less than 2 μm. Because light travels slower in tissue than in air, the optical delay is divided by the group velocity index of the tissue (*16*) to obtain the actual physical depth inside the tissue.

To acquire data for a two-dimensional image, a series of longitudinal scans are performed with the optical beam position translated laterally between scans. The lateral resolution of the image is limited by the beam diameter inside the sample. In our measurements, the beam diameter was 9 μm (FWHM). The two-dimensional scanning measurements map optical scattering as a function of depth and transverse position in an "optical section" of the tissue sample 9 μm thick, and the resulting data array can be viewed directly as a gray scale or false-color image. In contrast to x-ray computed tomography or magnetic resonance imaging, OCT does not require large amounts of computation for image reconstruction.

OCT can measure reflected signals with an extremely high detection sensitivity. Using only 20-μW incident optical power, the OCT system can detect reflections of $5 \times 10^{-10}$ of the incident optical power corresponding to a sensitivity of 10 fW. This high sensitivity is achieved by optical heterodyne detection. The interferometric signal is modulated at a high frequency by Doppler shift and piezoelectric modulation (Fig. 1). The interferometer output is then frequency-filtered in the demodulator to separate the desired interferometric signal from noise outside the signal bandwidth.

In order to demonstrate the feasibility of OCT, we examined two complementary systems: the peripapillary region of the retina and the coronary artery. The retina is a transparent layered structure with well-established morphological features. The arterial wall is a highly scattering turbid medium whose internal structure is normally obscured by scattering.

High-resolution imaging of retinal structure is clinically relevant for the diagnosis of a variety of diseases such as glaucoma, macular degeneration, and macular edema. The diagnosis and management of glaucoma are currently difficult clinical problems. Intraocular pressure measurements often do not adequately predict the progression of glaucoma (*17*). Loss of visual field and cupping of the optic nerve head may be late clinical findings detected only after up to 50% of retinal nerve fibers have been lost (*18*). New diagnostic techniques that measure properties of the retinal nerve fiber layer (RNFL) (*19*), retinal thickness (*20*), and contour changes in the optical disk (*21*) are being actively pursued. Because of its high resolution, OCT may be a sensitive method for the detection of these anatomic changes.

Figure 2A shows an OCT image of the retina and optic disk of the human eye. The morphological features of the OCT image directly correspond to histological findings (Fig. 2B). OCT scanning was performed after the removal of cornea and lens to simplify beam positioning. In the intact eye, the same measurement could be carried out with a beam-positioning system similar to that used in the scanning laser ophthalmoscope (*14*).

The RNFL, the anatomic structure that is affected in glaucoma, can be identified in the OCT image. The RNFL is a relatively highly scattering layer compared to the vitreous and the subjacent retinal structures. Because of the cylindrical nature of the nerve fibers, the strength of the backscattered signal from the RNFL is expected to be strongly dependent on the incident angle of the light (*22*). This angle dependence accounts for the attenuation of the RNFL signal that is observed at the margin of the optic disk where the nerve fibers descend into the optic nerve.

The tomograph in Fig. 2 images the retina and optic disk with higher depth resolution than can be obtained from clinical ultrasound or confocal scanning systems (*23*). It provides information on the contour and thickness of important retinal structures that can be the

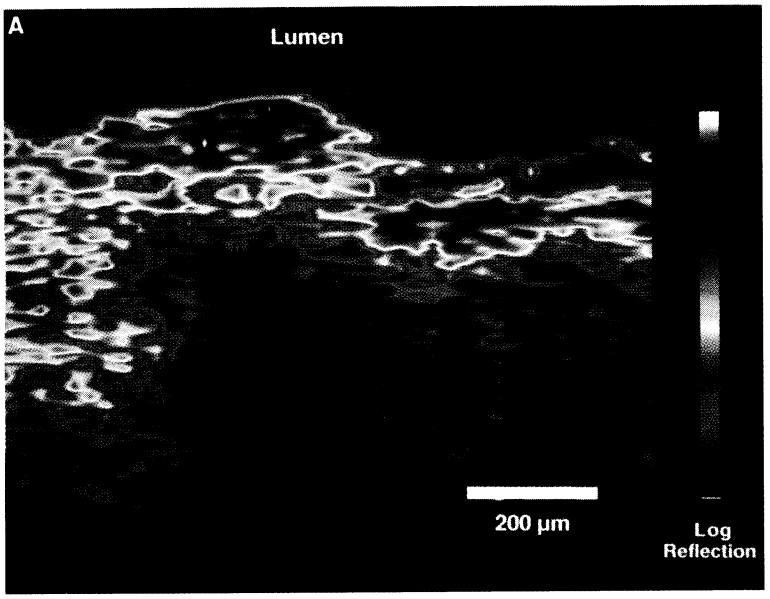


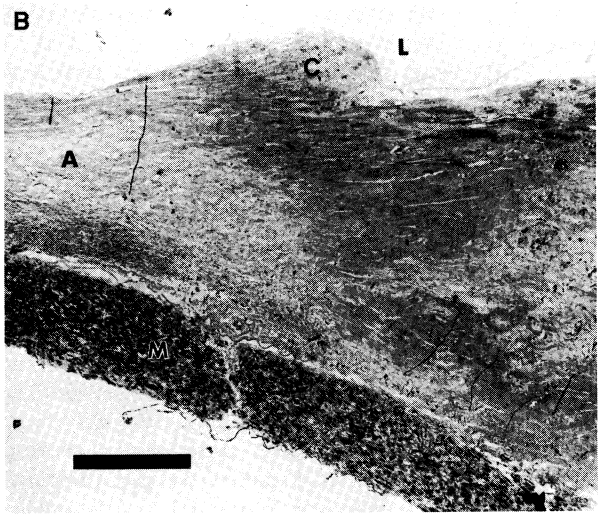


**Fig. 3.** Optical coherence tomographs of human coronary artery (A) and a histologic section of the same specimen (B). Artery specimens from a 68-year-old woman who died of myocardial infarction were obtained after autopsy and imaged before fixation. (**A**) The dissected specimen was maintained in saline, and the OCT beam was incident from the intimal surface. Fatty-calcified plaque (right three-quarters of image) backscatters and shadows the subjacent structures more strongly than fibroatheramatous plaque and normal arterial wall (left quarter). The sampled pixel size is 3.8 (vertical) by 25 (horizontal) μm. Interpolation between pixels was performed to improve image readability. The color scale spans $4 \times 10^{-10}$ (black) to $4 \times 10^{-5}$ (white) of the incident power. (**B**) Toluidine blue–stained plastic section. Lumen (L), fatty-calcified atherosclerotic plaque (C), fibroatheromatous plaque (A), media (M). Bar = 200 μm.

basis of new clinical diagnostic procedures. For example, quantitative assessment of the RNFL thickness would be a major advance in the management of glaucoma, a disease for which there is no objective test for the evaluation of disease progression.

The coronary arterial wall is another clinically important tissue that can be examined by OCT. Laser angioplasty and other technologies for the removal of vascular obstructions in the heart and other organs have been limited by poor delineation of pathologic and healthy tissues. OCT offers a method for probing the vessel wall in both open surgical and catheter-based vascular surgeries.

In the OCT image of coronary artery (Fig. 3), fatty-calcified plaque and fibroatheromatous plaque-normal arterial wall were contrasted by the larger backscattering and shadowing effect in the fatty-calcified plaque; near the intimal surface, the backscattered light was, on the average, roughly $3 \times 10^{-6}$ of the incident power in the fatty-calcified material and $2 \times 10^{-7}$ in the fibrous connective tissue. Because 830-nm light is poorly absorbed in tissue, the shadowing or attenuation of signal with depth is mainly due to scattering (*24*). In the fatty-calcified material, attenuation is rapid and the signal falls to near noise level within 150 to 200 μm. In the fibrous connective tissue, the signal was only attenuated by roughly a factor of 3 in the full 500-μm vessel wall thickness. The very weak signal ($<10^{-8}$ of the incident power) at distances below the specimen may be attributed to ghost echo effects from multiple scattering in the arterial wall.

Our ability to distinguish with OCT between the two types of turbid tissues in Fig. 3 suggests that this technique may be useful in both endoscopic and open surgical procedures in a wide variety of tissue. The ability to distinguish between normal arterial wall and atherosclerotic plaques could be important in guiding laser or other devices in intra-arterial angioplasty techniques. The fiber optic light path in the OCT scanner can potentially be coupled to optical fiber or fiber bundles in an endoscopic system.

The data acquisition time for the images shown here was determined by the longitudinal scan rate of 1.6 mm $s^{-1}$. For a wide-field image consisting of 150 longitudinal scans of 2 mm depth (Fig. 2A), the minimum image acquisition time is ~190 s. The acquisition rate is ultimately limited by the trade-off between signal bandwidth and detection sensitivity. If the incident optical power is increased up to 200 μW [the ANSI safe ocular exposure standard (*25*)] and the system is optimized to perform with near optical shot noise–limited detection (*26*), an OCT image like that shown in Fig. 2A can be acquired in 200 ms. Smaller or coarser grain images with fewer pixels can be acquired proportionately faster. Thus, measurement times shorter than the time scale of biological motion can be realized. In nonocular applications, much higher incident power can be used to shorten data acquisition time or increase signal level and penetration range.

The nature of the reflecting or backscattering structures in the biological sample places some practical limitations on OCT. Measurements of specular surfaces (refractive index discontinuity at the vitreoretinal boundary) and cylindrical reflectors (retinal nerve fibers) require angular alignment of the OCT system to achieve near normal incidence. Diffuse backscattering from tissue heterogeneity (vascular wall and internal retinal structures) has weaker angular dependence, and the detected signal level can be improved with the use of large numerical apertures. The presence of speckle noise will prevent the detection of subtle differences in tissue backscattering properties. In turbid media such as the vascular wall, multiply scattered light (echoes) retains sufficient coherence to be detected by the OCT system. These echoes will limit the depth range of OCT in situations where scattering predominates over absorption (*27*).

Because OCT is an optical method, a variety of optical properties can be utilized to identify tissue structure and composition. Directionally oriented tissues such as the elastic lamina of arteries and the RNFL are birefringent. OCT can analyze the polarization of reflected light in order to enhance the differentiation of birefringent tissue structures. OCT systems can also operate at multiple wavelengths in order to measure spectral properties. Properties such as chromaphore content, oxygenation of hemoglobin, hydration, or the size of light-scattering structures can be detected by spectral mea-

surements. Thus, OCT is a promising technique for both basic research and clinical applications.

REFERENCES AND NOTES


1. G. N. Houndsfield, *Br. J. Radiol.* **46**, 1016 (1973).
2. R. Damadian, M. Goldsmith, L. Minkoff, *Physiol. Chem. Phys.* **9**, 97 (1977).
3. J. J. Wild and J. M. Reid, *Science* **115**, 226 (1952).
4. B. Chance *et al.*, *Proc. Natl. Acad. Sci. U.S.A.* **85**, 4971 (1988).
5. J. G. Fujimoto *et al.*, *Opt. Lett.* **11**, 150 (1986); D. Stern *et al.*, *Inv. Ophthalmol. Vis. Sci.* **30**, 99 (1989).
6. K. G. Spears *et al.*, *IEEE Trans. Biomed. Eng.* **36**, 1210 (1989); H. Chen *et al.*, *Opt. Lett.* **16**, 487 (1991).
7. S. Andersson-Engels *et al.*, *Opt. Lett.* **15**, 1179 (1990); L. Wang, P. P. Ho, C. Liu, G. Zhang, R. R. Alfano, *Science* **253**, 769 (1991).
8. R. C. Youngquist, S. Carr, D. E. M. Davies, *Opt. Lett.* **12**, 158 (1987); K. Takada *et al.*, *Appl. Opt.* **26**, 1603 (1987).
9. G. S. Kino and S. S. C. Chim, *Appl. Opt.* **29**, 3775 (1990); B. S. Lee and T. C. Strand, *ibid.*, p. 3784.
10. A. F. Fercher, K. Mengedoht, W. Werner, *Opt. Lett.* **13**, 186 (1988); C. K. Hitzenberger, *Inv. Ophthalmol. Vis. Sci.* **32**, 616 (1991).
11. D. Huang *et al.*, *Lasers Surg. Med.* **11**, 5 (1991).
12. H. H. Gilgen *et al.*, *J. Lightwave Technol.* **7**, 1255 (1989).
13. P. Davidovits and M. D. Egger, *Appl. Opt.* **10**, 1615 (1971).
14. R. B. Webb, G. W. Hughes, F. C. Delori, *ibid.* **26**, 1492 (1987).
15. T. Wilson and C. Sheppard, *Theory and Practice of Scanning Optical Microscopy* (Academic Press, London, 1984).
16. The refractive index is used because it closely approximates group index. The retinal refractive index of 1.36 is found in D. R. Williams, *Inv. Ophthalmol. Vis. Sci.* **19**, 653 (1980). The same value is used in other tissues.
17. A. Sommer, *Am. J. Ophthalmol.* **107**, 186 (1989).
18. H. A. Quigley and E. M. Addicks, *Arch. Ophthalmol.* **100**, 807 (1982); H. A. Quigley, *Trans. Am. Ophthalmol. Soc.* **84**, 920 (1986); H. A. Quigley, G. R. Dunkelberger, W. R. Green, *Am. J. Ophthalmol.* **107**, 453 (1989).
19. A. Sommer *et al.*, *Arch. Ophthalmol.* **109**, 77 (1991); R. N. Weinreb *et al.*, *ibid.* **108**, 557 (1990); L. F. Jindra *et al.*, *Ophthalmic Surg.* **20**, 370 (1989).
20. R. C. Zeimer *et al.*, *Arch. Ophthalmol.* **107**, 1006 (1989); T. Takenori and B. Schwartz, *Ophthalmology* **96**, 1315 (1989).
21. F. E. Kruse *et al.*, *Ophthalmology* **96**, 1320 (1989); R. N. Weinreb, A. W. Dreher, J. F. Bille, *Int. Ophthalmol.* **13**, 25 (1989).
22. R. W. Knighton, S. G. Jacobson, C. M. Kemp, *Inv. Ophthalmol. Vis. Sci.* **30**, 2393 (1989).
23. The resolution of ultrasound is limited by the relatively long wavelengths needed for tissue penetration. Clinical ocular ultrasound typically uses 10-MHz ultrasound, which has a wavelength of 150 μm in tissue. The depth resolution of confocal laser scanning systems is limited by the aberration in ocular optics to roughly 200 μm (FWHM) according to J. F. Bille, A. W. Dreher, and G. Zinser, *Noninvasive Diagnostic Techniques in Ophthalmology*, B. R. Masters, Ed. (Springer-Verlag, Berlin, 1990), p. 528.
24. S. L. Jacques, *IEEE Trans. Biomed. Eng.* **36**, 1155 (1989).
25. The ocular safe exposure standard for permanent intrabeam viewing of 830-nm light with full 7-mm pupil aperture. ANSI Z136 (American National Standards Institute, 1986).
26. H. A. Haus, *Waves and Fields in Optoelectronics* (Prentice-Hall, Englewood Cliffs, NJ, 1984), p. 379.
27. K. M. Yoo, F. Liu, R. R. Alfano, *Opt. Lett.* **16**, 1068 (1991).
28. C. P. Lin, J. S. Schuman, and C. A. Puliafito are presently with the Department of Ophthalmology, Tufts University School of Medicine, Boston, MA 02111. We thank T. F. Deutsch and R. Birngruber for helpful discussions, and we thank W. J. Woods for technical assistance. This work was supported by National Institutes of Health contract 1-R01-GM35459-06 and Office of Naval Research contract N-00014-91-J-1956.


1 August 1991; accepted 23 September 1991

# Cooperative Solution of Constraint Satisfaction Problems

SCOTT H. CLEARWATER, BERNARDO A. HUBERMAN, TAD HOGG

**It is widely believed that a group of cooperating agents engaged in problem solving can solve a task faster than either a single agent or the same group of agents working in isolation from each other. Nevertheless, little is known about the quantitative improvements that result from cooperation. A number of experimental results are presented on constraint satisfaction that both test the predictions of a theory of cooperative problem solving and assess the value of cooperation for this class of problems. These experiments suggest an alternative methodology to existing techniques for solving constraint satisfaction problems in computer science and distributed artificial intelligence.**

THAT COOPERATION LEADS TO IMprovements in the performance of a group of individuals underlies the founding of a firm, the existence of scientific and professional communities, and the establishing of committees charged with solving particular problems. In computation, the emergence of massively parallel machines underscores the assumed power of concurrency for solving very complex tasks that can be decomposed into smaller pieces, and a large effort is being devoted to the design of parallel algorithms for the solution of computationally hard problems.

Many of these tasks can be viewed as searches in large problem spaces. For realistic problems, where no algorithmic solution is known, heuristic methods are used to prune the search. Moreover, even with massively parallel machines, the huge size of the search space means that there will still be a large amount of search per processor. Recently, a theory that elucidates the performance of cooperative processes searching through a large problem space was developed (*1*). It showed that cooperative searches, when sufficiently large, can display universal characteristics, independent of the detailed nature of either the individual processes or the particular problem being tackled. This universality manifests itself in two separate ways: first, the existence of a sharp transition from exponential to polynomial time required to find the solution as heuristic effectiveness is improved (*2*); second, the appearance of a lognormal distribution in the effectiveness of an individual agent's problem solving. The enhanced tail of this distribution guarantees the existence of some agents with superior performance. This can bring about a combinatorial implosion (*3*) with superlinear speedup in the time to find the answer with respect to the number of processes.

We present a number of experimental results on cooperative problem solving that both test the predictions of the theory and provide a quantitative assessment of the value of cooperation in solving a class of problems. These experiments were carried out by having a number of computational agents solve a set of cryptarithmetic problems and measuring their individual and global performance. These results provide a striking example of the improvements in performance that result from cooperation and suggest an alternative methodology to existing techniques for solving constraint satisfaction problems in computer science and distributed artificial intelligence (*4*).

Cryptarithmetic codes are typical of constraint satisfaction problems that lie at the heart of studies of human and computer problem solving (*5, 6*). The task is to find unique digit assignments to each of the letters so that the numbers represented by the words add up correctly. The constraint of a unique digit for a unique letter in a decimal representation reduces the total number of possible states, $N_{\text{states}}$, from $10^n$ to $10!/(10 - n)!$ where $n$ is the number of unique letters in the problem. A familiar example of such problems is provided by the sum: *DONALD* + *GERALD* = *ROBERT*. This particular problem has $n = 10$ and one solution, which is given by $A = 4$, $B = 3$, $D = 5$, $E = 9$, $G = 1$, $L = 8$, $N =$

Dynamics of Computation Group, Xerox Palo Alto Research Center, Palo Alto, CA 94304.